nature communications

Article

https://doi.org/10.1038/s41467-023-42492-z

Enabling giant thermopower by heterostructure engineering of hydrated vanadium pentoxide for zinc ion thermal charging cells

Received: 3 April 2023

Accepted: 12 October 2023

Zhiwei Li[1], Yinghong Xu[1], Langyuan Wu[1], Jiaxin Cui[1], Hui Dou[1] &
Xiaogang Zhang[1]

Flexible power supply devices provide possibilities for wearable electronics in the Internet of Things. However, unsatisfying capacity or lifetime of typical batteries or capacitors seriously limit their practical applications. Different from conventional heat-to-electricity generators, zinc ion thermal charging cells has been a competitive candidate for the self-power supply solution, but the lack of promising cathode materials has restricted the achievement of promising performances. Herein, we propose an attractive cathode material by rational heterostructure engineering of hydrated vanadium pentoxide. Owing to the integration of thermodiffusion and thermoextraction effects, the thermopower is significantly improved from 7.8 ± 2.6 mV K^{-1} to 23.4 ± 1.5 mV K^{-1}. Moreover, an impressive normalized power density of 1.9 mW m^{-2} K^{-2} is achieved in the quasi-solid-state cells. In addition, a wearable power supply constructed by three units can drive the commercial health monitoring system by harvesting body heat. This work demonstrates the effectiveness of electrodes design for wearable thermoelectric applications.

Portable devices are widely used in wearable applications for communication, health monitoring, and other areas. However, the unsatisfying capacity and lifetime of power systems like batteries and supercapacitors seriously hinder the development of wearable electronics[1,2]. Under this consideration, power supply systems with characteristics of low-cost, high performance, sustainability, and good durability are extremely necessary for the construction of Internet of Things (IoTs)[3–6]. Thermoelectric devices (TEs), as one of the key techniques, can directly convert low-grade heat into electricity under a low temperature difference of several Kelvins based on the Seebeck effect, which provides in principle the practicability of TEs in self-power supply for electronics using human body heat[7–10]. Very recently, Qiu and his co-workers discovered a series of p-type ductile TE materials, AgCu(Se, S, Te) pseudoternary solid solutions for the fabrication of flexible TEs[11]. When coupling with the n-type ductile material ($Ag_{20}S_7Te_3$), they developed a π-type flexible TE devices with a thickness of 0.3 mm and high normalized power density of 30 μW cm^{-2} K^{-2}. It should point out that this device-integrated 31-pair flexible TE units adhered to human's wrist can output a voltage of 0.2 mV and power of 70 nW. Although some applied heat-dissipation routes like copper pipes and graphite sheets would further improve the output performances to power some microelectronics, the relatively complicated integration of working units still is the key issue that needs to be addressed.

Alternatively, ionic thermoelectric devices (i-TEs) are proposed for low-grade heat harvesting by combining the diffusion of ions and redox reactions of species under the existence of temperature gradient[12,13]. Owing to the rational integration of thermodiffusion and

---

[1] Jiangsu Key Laboratory of Electrochemical Energy Storage Technologies, College of Material Science and Technology, Nanjing University of Aeronautics and Astronautics, Nanjing 211106, China. e-mail: azhangxg@nuaa.edu.cn

thermogalvanic effects, i-TEs have been widely concerned by researchers in practical applications[14]. As a proof-of-concept, Liu et al. developed a new-type ionic thermoelectric material for the harvesting of human body heat[15]. Typically, potassium chloride (KCl) and ferro/ferricyanide [$Fe(CN)_6^{4-}$/$Fe(CN)_6^{3-}$] were optimized in a gelatin matrix to simultaneously achieve the synergistic changes of thermodiffusion entropy and thermogalvanic entropy. As a result, a giant thermopower of 17.0 mV K^{-1} can be obtained using copper electrode under a temperature difference of ~10 K. Most importantly, a high voltage of 2 V and a peak power of 5 mW can be generated from the harvesting of body heat by integrating 25 unipolar units. Huang et al. designed a nonaqueous ionogel with strong ion-ion interactions introduced by selective ion doping to adjust the ionic thermopower[16]. Detailly, ionogels based on an ionic liquid (EMIMTFSI/PVDF-HFP) shows high negative thermopower of −15 mV K^{-1} after adding 0.5 M $LiBF_4$. Moreover, a peak value of positive thermopower (17 mV K^{-1}) can be achieved with the introduction of EMIMCl. According to these inspired results, the prototype device with 12 pairs of n-/p-type units, which is adhered on human arm, can produce a voltage of 0.33 V. Apart from the development of advanced ionogels, the introduction of chaotropic/host agent is an efficient strategy to enhance the thermoelectrochemical performances by increasing the concentration difference[17]. For example, Zhou and co-workers reported a thermosensitive guanidinium (Gdm^+) induced $Fe(CN)_6^{4-}$ crystallization to construct high-performance thermocells[18]. With the precipitation of crystals, both the voltage and thermopower of the system can be enhanced. However, it is difficult to adopt the precipitation and redissolution of thermosensitive crystallization into wearable applications that would meet the demands of multidimensional motion. Till now, the development of high-performance thermoelectric devices has been the top priority for self-powered electronics through human body heat harvesting.

Besides the optimization of functional electrolytes, electrode engineering is another efficient approach to improve thermoelectrochemical performances[19]. Based on the electrical double-layer capacitive effect or near-surface redox behavior, some electrode materials including porous carbon, carbon nanotube, and conductive polymer are widely studied in previous reports[20–26]. To further boost the energy conversion efficiency and energy storage density during the thermoelectrical process, we have proposed a zinc ion thermal charging cell (ZTCC) using Zn metal anode and vanadium dioxide-porous carbon (VO_2-PC) cathode[27]. As-fabricated ZTCC can convert low-grade heat into electricity with a thermopower of ~12.5 mV K^{-1} by the combination of thermodiffusion and thermoextraction. Notably, the whole thermoelectrochemical process is dominated by the thermodiffusion effect, which may be caused by the embedding feature of VO_2 in PC matrix. It should be mentioned that the average ion diffusion coefficient of VO_2-PC is in a relatively low level (3.16×10^{-11} cm^2 S^{-1}). To realize a fast thermoelectrochemical response of ZTCCs, the kinetics matching of themodiffusion and thermoextraction, as well as the ion mobility and conductivity of electrode materials, should be well considered. Importantly, vanadium oxides (especially for vanadium pentoxides) are regarded as attractive candidates for energy storage and conversion owing to their relatively large inner spacing, tuned nanostructures, and multielectron reactions[28,29]. Nonetheless, the dissolution of vanadium in neutral or acidic electrolytes during electrochemical processes would result in the failure of electrodes and contamination of electrolytes. Meanwhile, the low electronic conductivity and electrostatic repulsion of layered vanadium oxides always lead to unsatisfying rate/power performances.

Herein, we propose and demonstrate a ZTCC with boosted performances using graphite modified zinc anode (Zn-G) and vanadium pentaoxide@reduced graphene oxide (V_2O_5@rGO) cathode. In detail, the properties of V_2O_5 are reasonably adjusted by the addition of rGO. Benefitting from the thermodiffusion contribution of rGO and thermoextraction behavior of V_2O_5, high-performance ZTCC in term of thermopower and power density can be achieved. Worthily, the rGO nanosheets can not only enhance the kinetics of V_2O_5 host, but also suppress the dissolution of vanadium species. Such attractive integration between V_2O_5 and rGO endows as-prepared V_2O_5@rGO composites with high thermal and electrochemical stability. In addition, the V_2O_5@rGO-1.5 based ZTCC shows great promise in the application of wearable health monitoring systems. Compared with other strategies for designing flexible thermoelectric systems, this work provides a facile way to construct a boosted ionic thermoelectrochemical device by the efficient structure regulation of electrode materials.

Results

Boosted ZTCCs enabled by V_2O_5@rGO-x

ZTCC constructed by insertion-type cathode and zinc metal anode attracts great attention due to the promising thermoelectrochemical performances during the conversion of low-grade heat and energy storage. As schematically illustrated in Fig. 1a, the thermopower of ZTCC is mainly determined by the thermodiffusion of electrolyte ions and thermogalvanic processes of electrodes. In detail, the pre-inserted cations in the cathode can be gradually extracted with heat input and transferred to the anode side under the effect of the thermal field. With the plating of diffused Zn^{2+} in Zn anode, the heat energy can be converted into electricity and stored simultaneously. Fig. 1b displays the possible voltage curve. To achieve a boosted thermoelectrochemical response, the development of electrode materials with fast kinetics and good durability becomes significant. The combination of vanadium oxides with nanocarbons shows great promise to overcome such challenges. As a demo, we proposed the $V_2O_5{\cdot}1.6H_2O$ with large interlayer spacing as a host material for charge storage and rGO as a functional matrix to enhance the kinetics and stability of composites. The density functional theory (DFT) calculations were performed on the model structure to understand the relationship between the electronic structure of V_2O_5@rGO and the superior kinetics behavior. As shown in Fig. 1c, the differential charge density of V_2O_5@rGO displays obvious charge accumulation around the V and O atoms and dispersion of surrounding electron states around the Zn atom. This charge redistribution reveals the optimized electronegativity of $V_2O_5{\cdot}1.6H_2O$, further boosting the adsorption ability to Zn^{2+}. Consequently, the V_2O_5@rGO exhibits a low negative adsorption energy of Zn^{2+} (−1.47 eV). This suggests that the ultra-large interlayer spacing of $V_2O_5{\cdot}1.6H_2O$ is beneficial to the adsorption and diffusion of Zn^{2+}. Simultaneously, the crystal H_2O molecules in V_2O_5 layers can act as a "lubricant" to improve host electrochemical kinetics. Subsequently, the rGO layer on $V_2O_5{\cdot}1.6H_2O$ surface retains structural integrity and accelerates the charge transfer. In addition, the diffusion pathway of Zn^{2+} in the V_2O_5@rGO sample is shown in Fig. 1d. It is worth mentioning that the energy barrier for ions diffusion in V_2O_5@rGO is at a low level of 0.27 eV (Supplementary Fig. 1), confirming the easy diffusion of Zn^{2+} along the V_2O_5@rGO heterointerface. Such high Zn^{2+} diffusion coefficient and low diffusion barrier endow V_2O_5@rGO composites with high-power/rate performances in energy conversion and storage applications.

According to the guidelines, we propose an electrostatic interaction-induced self-assembly strategy to realize the structure regulation on the V_2O_5@rGO-x nanocomposites (x: concentration of GO solution, mg mL^{-1}). The field-emission scanning electron microscopy (FESEM) and transmission electron microscopy (TEM) images in Supplementary Fig. 2 and Fig. 1e clearly indicate that the V_2O_5@rGO-1.5 shows reasonably intertwined microstructure engineered by multilayer rGO and V_2O_5 nanobelts with several micrometers in length. It is worth mentioning that the 1D V_2O_5 nanobelts with large interlayer spacing can provide abundant electrochemical sites for ions intercalation/deintercalation and the 2D rGO nanosheets wrapped around the V_2O_5 nanobelts can act as matrix for ions adsorption/desorption as

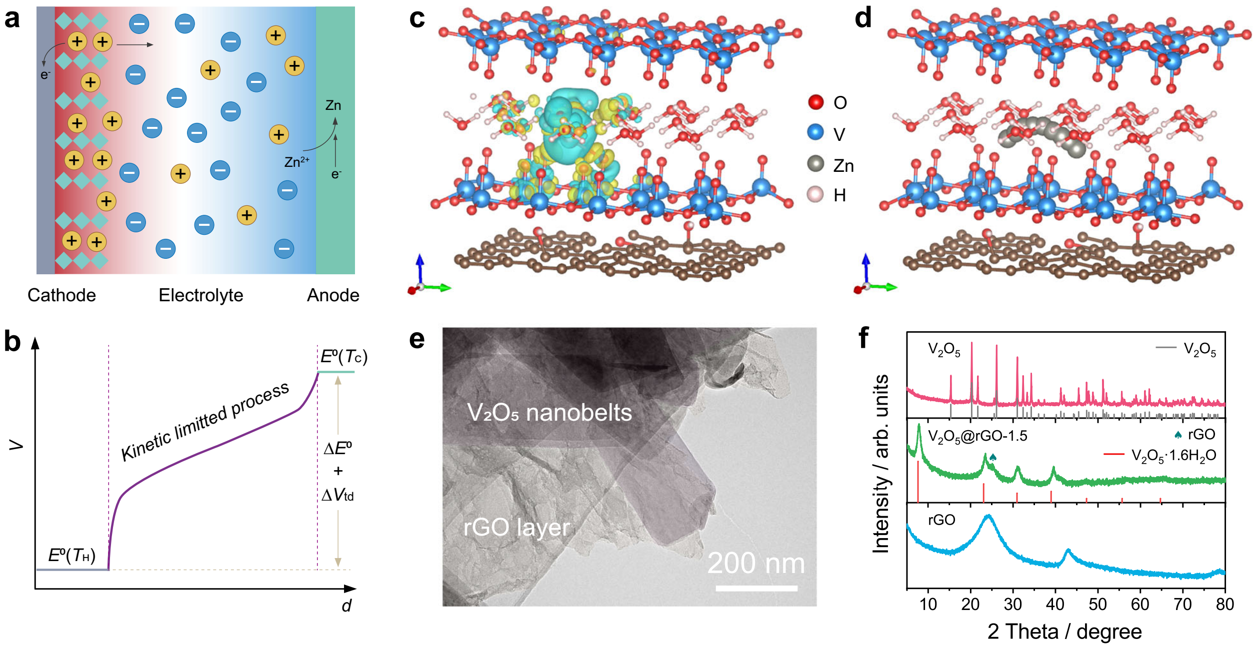

Fig. 1 | Construction of boosted ZTCC and characterization of V_2O_5@rGO sample. **a** Schematic illustration of V_2O_5@rGO based ZTCC, and **b** corresponding voltage distribution profile. **c** Differential charge density, and **d** the optimized diffusion pathway of Zn^{2+} in V_2O_5@rGO composite. **e** TEM image of V_2O_5@rGO-1.5. **f** XRD pattern of V_2O_5, V_2O_5@rGO-1.5, and rGO.

well as a pathway for charge transfer. However, the pure V_2O_5 obtained without adding GO solution exhibits random nanoparticle morphology (Supplementary Fig. 3a), which is significantly different from the nanobelt-type V_2O_5 in V_2O_5@rGO nanocomposites. Moreover, the pristine GO after hydrothermal process displays a well-developed 3D continuous framework formed by corrugated and stacked rGO nanosheets (Supplementary Fig. 3b). When considering the fully different microstructures of V_2O_5@rGO, V_2O_5, and rGO samples, it can be concluded that the introduction of GO into the preparation of V_2O_5 is a rational approach to regulate the structure of nanohybrids. In fact, the relatively acidic atmosphere (pH: ~3.0) caused by GO solution could promote the generation of positively vanadium oxide, which would adsorb on the negatively charged surface of GO and gradually evolve into nanobelts between rGO layers[30]. The morphologies of V_2O_5@rGO composites highly depend on the content of rGO. As displayed in Supplementary Fig. 3c, the V_2O_5@rGO-1.0 holds the characteristics of V_2O_5 nanobelts, in which rGO substrate is fully covered. While for the V_2O_5@rGO-2.0, only a few V_2O_5 nanobelts are exposed from the 3D graphene network (Supplementary Fig. 3d). The corresponding high-resolution transmission electron microscopy (HRTEM) image in Supplementary Fig. 4 confirms the successful synthesis of layered V_2O_5 in V_2O_5@rGO-1.5 sample. Consistently, the ultra large interlayer spacing of around 1.1 nm can be indexed to the (001) plane of orthorhombic $V_2O_5{\cdot}1.6H_2O$[31]. Selected area electron diffraction (SAED) pattern reveals the polycrystalline feature of formed $V_2O_5{\cdot}1.6H_2O$ nanobelts and amorphous rGO layers (Supplementary Fig. 5), further confirming the formation of heterostructure by $V_2O_5{\cdot}1.6H_2O$ and rGO. Meanwhile, the high-angle annular dark-field scanning transmission electron microscopy (HAADF-STEM) and corresponding elemental mapping images detect the distribution of V, C, and O elements in V_2O_5@rGO-1.5, demonstrating the rational integration of rGO and V_2O_5 (Supplementary Fig. 6).

The phase and structure of samples are confirmed by the X-ray diffraction (XRD) patterns. As plotted in Fig. 1f, all the obvious peaks of V_2O_5@rGO-1.5 correspond to the characteristic peaks of orthorhombic $V_2O_5{\cdot}1.6H_2O$ (PDF#40−1296). The additional peak around 25.3° in the spectrum of V_2O_5@rGO-1.5 can be attributed to the (002) plane of amorphous rGO. Interestingly, the pure V_2O_5 obtained without addition of GO is in terms of orthorhombic V_2O_5 (PDF#89-0612)[32]. Notably, the pattern of V_2O_5@rGO-1.0 is similar with that of V_2O_5@rGO-1.5 (Supplementary Fig. 7). The interlayer spacing of pure V_2O_5 is significantly enlarged from ~0.44 nm to ~1.1 nm of $V_2O_5{\cdot}1.6H_2O$ in both V_2O_5@rGO-1.5 and V_2O_5@rGO-1.0, implying that acidic GO exhibits important role in regulating the microstructure of vanadium oxides. Moreover, as detected by the XRD pattern of V_2O_5@rGO-2.0, the $V_2O_5{\cdot}1.6H_2O$ crystals can further evolve into low-valence vanadium species like V_6O_{13} and $V_3O_7{\cdot}1.6H_2O$ with the increasing of GO concentration due to partial reduction of high-valence vanadium species by formed rGO during hydrothermal treatment. The comparison of Raman spectra in Supplementary Fig. 8 shows typical characteristics of rGO (1330.7 and 1598.2 cm^{-1}) and VO_x (142.5, 194.4, 662.2, 404.8, 698.2 and 992.7 cm^{-1})[33,34]. The co-existence of above Raman peaks in V_2O_5@rGO-x hybrid demonstrates the rational combination of rGO and VO_x, further confirming the composition of the heterostructure. Moreover, the thermogravimetric analysis (TGA) indicates that the V_2O_5 in V_2O_5@rGO-1.5 contains ~1.62 crystal water molecules per unit, and the content of rGO is about 31.7% (Supplementary Fig. 9). In addition, the specific surface area (SSA) of sample is measured by N_2 adsorption-desorption isotherms (Supplementary Fig. 10a). Benefitting to the abundant pores and 3D-interconnected structure, the rGO shows the largest adsorbed quantity among as-prepared materials. Consequently, a high SSA value of 284.1 $m^2\ g^{-1}$ can be achieved (Supplementary Fig. 10b). However, the pristine V_2O_5 only shows 5.2 $m^2\ g^{-1}$. After introducing rGO, the SSA value can be reasonably improved to 13.3 $m^2\ g^{-1}$ for V_2O_5@rGO-1.5. Such high SSA together with mesoporous feature of V_2O_5@rGO-1.5 can effectively boost the ions mobility. The X-ray photoelectron spectroscopy (XPS) of V_2O_5, rGO and V_2O_5@rGO-x composites was carried out to reveal the integration of carbon matrix and vanadium oxides (Supplementary Fig. 11a). Notably, the broad peak of O 1*s* for V_2O_5 at 530.3 eV can be attributed to the VO_x (Supplementary Fig. 11b)[35]. Deconvolution of O 1*s* spectra for V_2O_5@rGO-x samples shows two additional peaks at 531.4 and 533.4 eV, which corresponds to the C = O groups in rGO and the water in the sample, respectively[35,36]. As shown in Supplementary Fig. 11c, the peaks at 517.3

(V $2p_{3/2}$) and 524.6 eV (V $2p_{1/2}$) for V_2O_5 belong to V^{5+}[37]. After combining with rGO, a part of V^{4+} can be found in V 2*p* of V_2O_5@rGO-x composites. Detailly, the ratio of V^{4+} to V^{5+} gradually increases from 0.28 (V_2O_5@rGO-1.0) to 0.47 (V_2O_5@rGO-2.0), which could be caused by the reduction effect of rGO to V^{5+} during the hydrothermal procedure. Moreover, the contact angle (CA) of pristine V_2O_5 is about 26.1° (Supplementary Fig. 12a), suggesting its superhydrophilic feature. Even after standing 20 s, the CA value still can be maintained at 23.2° (Supplementary Fig. 12b). Worthily, the CA value of V_2O_5@rGO-x composite gradually increases with the increase of rGO amount, which may be caused by the stack of graphene layers. According to the change of CA values during electrolyte immersion, the V_2O_5@rGO-1.0 delivers higher electrolyte permeability than that of V_2O_5@rGO-1.5 and V_2O_5@rGO-2.0. These differences in CA values highly affect to the dissolution of vanadium species from the electrode into the electrolyte. As shown in Supplementary Fig. 13a, the electrolyte solution with pristine V_2O_5 shows a noticeable color change from transparent to yellow, suggesting the serious dissolution of V species in the electrolyte. As expected, the dissolution of V species of various V_2O_5@rGO-x electrodes can be significantly suppressed by the rGO coating layers. Furthermore, the detailed concentration of V species in electrolytes after soaking for 5 days and 10 days is summarized in Supplementary Fig. 13b. After soaking for 5 days, the concentration of V in electrolyte for V_2O_5 is 47.5 mg L^{-1}, which is several times higher than those for V_2O_5@rGO-x electrodes (8.9 ~ 17.3 mg L^{-1}). Even after soaking for 10 days, the average V element dissolution rate of V_2O_5 (7.1 mg L^{-1} per day) is much higher than those of V_2O_5@rGO-x electrodes (1.1 ~ 2.0 mg L^{-1} per day), confirming the important role of rGO to maintain the structure stability in V_2O_5@rGO-x composites. Besides, the ultralow electron conductivity of 1.4×10^{-5} S cm^{-1} for pristine V_2O_5 can be significantly enhanced to 1.2 S cm^{-1} for the V_2O_5@rGO-1.5 with the introduction of rGO (Supplementary Fig. 14). Thus, the coated rGO on V_2O_5 nanobelts can be acted as conductive layers in heterostructure to enhance the kinetics as well as satisfying power capability in energy conversion and storage.

Evaluation of thermoelectrochemical performances

To correlate the structure regulation of V_2O_5@rGO-x with the enhancement of thermoelectrochemical performances in the harvesting of low-grade heat, the open-circuit voltage values of systems were recorded using non-isothermal H-type cell. Detailly, the modified Zn-G foil (thickness: ~20 μm) and V_2O_5@rGO-x are used as anode in cold side and cathode on hot side, respectively. It should be pointed out that the temperature difference (Δ*T*) between such two chambers can be formed by water bath and determined by inserted thermocouples. To evaluate the Seebeck coefficient of rGO, V_2O_5, V_2O_5@rGO-1.0, V_2O_5@rGO-1.5, and V_2O_5@rGO-2.0, we have profiled the related results with error bands or error bars (error band/bar represents the standard deviations). Benefitting to the adsorption/desorption mechanism of ions, the kinetics of V_2O_5 can be rationally enhanced with the addition of rGO. As summarized in Fig. 2a, the V_2O_5@rGO-1.5 based ZTCC generated the highest output voltage of ~1.1 V among all other ZTCCs. In fact, such high voltage can be divided as thermal-induced voltage and self-charging-induced voltage. The self-charging

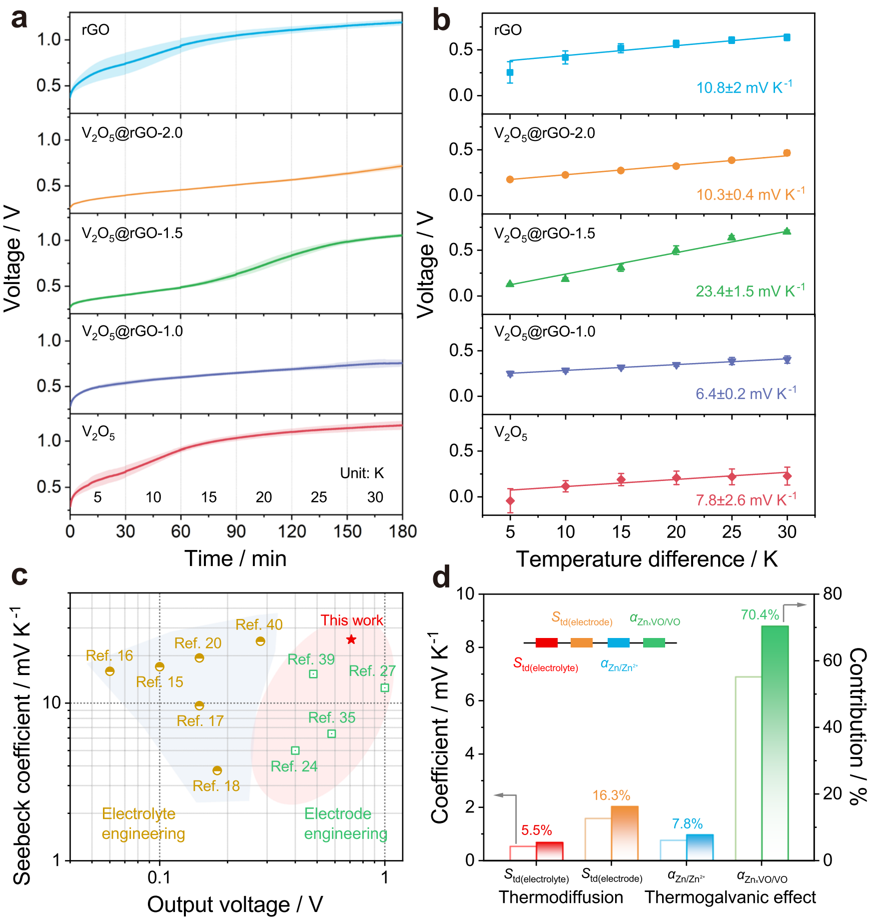

Fig. 2 | Thermoelectrochemical performances of H-type ZTCCs using 0.5 mol L^{-1} $Zn(CF_3SO_3)_2$. a Output voltage under various temperature differences from 5 K to 30 K, and **b** corresponding Seebeck coefficient. **c** Comparison of Seebeck coefficient and thermal-induced voltage with other reported values. **d** Temperature coefficients and corresponding fractional contributions of various thermal processes.

behavior of Zn-related devices was carefully studied in previous works[38]. To exclude the contribution of the self-charge process to the total voltage, we further recorded the voltage curves during self-charging processes in Supplementary Fig. 15. Owing to the continuous and dense framework of rGO, the gradual desorption of ion from interconnected channels endows rGO-contained ZTCC with relatively low self-charging rate. Thus, the V_2O_5@rGO-1.5 based ZTCC delivers the highest thermal-induced voltage of 0.72 V. Based on these results, the thermopower or Seebeck coefficient (S_i) can be determined by the relationship between thermal-induced voltage and temperature difference[15,18]:

$$S_i = \frac{\Delta V}{\Delta T} \tag{1}$$

As profiled in Fig. 2b, the rGO-based ZTCC shows large S_i value of $10.8 \pm 2\,\mathrm{mV\,K^{-1}}$ based on the ultrafast adsorption/desorption. While the V_2O_5 based ZTCC only delivers $7.8 \pm 2.6\,\mathrm{mV\,K^{-1}}$ due to the relatively sluggish insertion/extraction of Zn^{2+} in its crystalline layers. When combining the merits of rGO and V_2O_5, a giant S_i value of $23.4 \pm 1.5\,\mathrm{mV\,K^{-1}}$ can be rationally achieved by adjusting the content of rGO. In detail, the slight lower S_i value of V_2O_5@rGO-1.0 based ZTCC than that of V_2O_5 based ZTCC may result from the its relatively dense structure and relatively low specific surface area. While for V_2O_5@rGO-2.0 based ZTCC, the S_i value is close to that of rGO-based ZTCC, which may be caused by the stacking of as-introduced excessive rGO into V_2O_5. Accordingly, the Seebeck coefficient highly depends on the synergy behavior of thermal adsorption/desorption and thermal insertion/extraction. As is compared in Fig. 2c, this breakthrough is also superior to most of previously reported results[15–18,20,23,24,27,35,39,40], indicating the great promise of structure regulation by integrating graphene and vanadium oxides for high-efficient conversion from heat to electricity. As profiled in Supplementary Fig. 16, the rGO, V_2O_5, V_2O_5@rGO-1.0, V_2O_5@rGO-1.5, and V_2O_5@rGO-2.0 based ZTCC exhibits thermo-voltage of approximately 1.2, 1.2, 0.75, 1.1, and 0.7 V with the temperature difference of 30 K. It is worth mentioning that such output voltage can be further enhanced to 1.6 V by adding power charge. After discharging with a current density of $0.1\,\mathrm{A\,g^{-1}}$, we can calculate that the ratio of thermal charge part in fully charged rGO, V_2O_5, V_2O_5@rGO-1.0, V_2O_5@rGO-1.5, and V_2O_5@rGO-2.0 based cell is 55.2%, 68.3%, 41.2%, 69.3%, and 30.0%, respectively. This result indicates that the heat-to-current conversion of ZTCC is highly determined by the kinetics of electrodes. Supplementary Fig. 17 displays the short-circuit current plots and fitted power density curves under thermal-induced voltage for various H-type ZTCCs. As found, the V_2O_5@rGO-1.5 based ZTCC delivers high voltage of 0.67 V and current density of $5.3\,\mathrm{A\,m^{-2}}$ among rGO (0.39 V, $0.42\,\mathrm{A\,m^{-2}}$), V_2O_5 (0.41 V, $0.59\,\mathrm{A\,m^{-2}}$), V_2O_5@rGO-1.0 (0.59 V, $1.7\,\mathrm{A\,m^{-2}}$), and V_2O_5@rGO-2.0 (0.59 V, $3.5\,\mathrm{A\,m^{-2}}$). Further, a relatively low resistance value of 1118.7 Ω can be calculated from the V_2O_5@rGO-1.5 based ZTCC, while the value is 3071.3 and 1491.8 Ω for V_2O_5@rGO-1.0 and V_2O_5@rGO-2.0, respectively. Besides, the rGO based ZTCC delivers relatively high inner resistance of 8217 Ω due to its poor wettability for electrolyte. While the resistance of 6150 Ω for V_2O_5 based ZTCC is mainly caused by its ultralow electron conductivity. Meanwhile, the V_2O_5@rGO-1.5 based ZTCC exhibits an excellent thermal-induced power density of $0.94\,\mathrm{W\,m^{-2}}$, meaning a high $P_{max}/(A \times \Delta T^2)$ value of $1.04\,\mathrm{mW\,m^{-2}\,K^{-2}}$. Such values are greatly larger than that of $0.06\,\mathrm{W\,m^{-2}}$ ($0.07\,\mathrm{mW\,m^{-2}\,K^{-2}}$), $0.06\,\mathrm{W\,m^{-2}}$ ($0.07\,\mathrm{mW\,m^{-2}\,K^{-2}}$), $0.27\,\mathrm{W\,m^{-2}}$ ($0.3\,\mathrm{mW\,m^{-2}\,K^{-2}}$), and $0.65\,\mathrm{W\,m^{-2}}$ ($0.72\,\mathrm{mW\,m^{-2}\,K^{-2}}$) for rGO, V_2O_5, V_2O_5@rGO-1.0 and V_2O_5@rGO-2.0 based ZTCCs, respectively. As shown in Supplementary Fig. 18, the V_2O_5@rGO-1.5 based ZTCC maintains relatively stable voltage change over 6000 s (60 cycles), demonstrating its good thermal charging stability. Due to the mismatched energy/kinetics during thermoelectrochemical process, the dramatic change in the voltage during the tests can be found in the rGO, V_2O_5, V_2O_5@rGO-1.0, and V_2O_5@rGO-2.0 based ZTCCs. Moreover, a negligible voltage drop (7 ~ 29 mV) occurs in self-discharge curves of various H-type ZTCCs when eliminating the temperature gradient (Supplementary Fig. 19). Especially, the V_2O_5@rGO-x based ZTCCs show relatively fast thermoelectrochemical response, and V_2O_5@rGO-1.5 based ZTCC delivers the lowest voltage change of ~7 mV, suggesting the dense energy storage behavior of as-proposed ZTCC. The gradual growth of voltage in following process can be attributed to the chemically self-charging behaviors[38]. To detailly study the relative contribution of thermodiffusion and thermogalvanic process to such giant value, we conducted a series of measurements for various temperature coefficients from 25 to 50 °C using the three-electrode configuration proposed in previous works[17,35]. As briefly illustrated in Supplementary Fig. 20a, two same electrodes are employed as working electrode and counter electrode, respectively, and the Ag/AgCl is used as reference electrode. During tests, the temperature of setup is determined by hot water bath and recorded by thermocouple. As plotted in Supplementary Fig. 20b, the thermodiffusion of electrolyte ions can deliver a temperature coefficient of $0.54\,\mathrm{mV\,K^{-1}}$. Notably, the temperature coefficient for Zn/Zn^{2+} and Zn_xVO/VO is 0.77 and $6.9\,\mathrm{mV\,K^{-1}}$ (Supplementary Fig. 20c–f), respectively. Consequently, the total temperature coefficient ($9.8\,\mathrm{mV\,K^{-1}}$) can be divided as 21.8% of thermodiffusion contribution and 78.2% of electronic effect contribution (Fig. 2d). All these findings reveal that the rational integration of capacitor-type rGO and battery-type V_2O_5 can realize the ultrafast response to heat/electricity signal.

Kinetics analyses

The kinetics of as-obtained V_2O_5@rGO-1.5 cathode was reasonably studied by the cyclic voltammetry (CV) measurements and the galvanostatic intermittent titration techniques (GITT) with an operating voltage window from 0.2 to 1.6 V (Supplementary Note 1, Supplementary Figs. 21 and 22). As displayed in Fig. 3a, two pair of visible redox peaks at 0.4/0.7 V and 0.9/1.1 V in all the CV curves from 0.1 to $1.0\,\mathrm{mV\,s^{-1}}$ can be attributed to the multiple insertion/extraction procedures of Zn^{2+} in V_2O_5 ($V_2O_5 + xZn^{2+} + yH_2O + 2xe^- \leftrightarrow Zn_xV_2O_5{\cdot}yH_2O$). The well-maintained CV curves even at relatively high scan rate further suggest the good reversibility and rapid response of V_2O_5@rGO-1.5 electrode. As one of convenient indicators, the near surface-dominated procedure and bulk diffusion-controlled process can be distinguished by using $i = a\upsilon^b$, where i and υ represent the peak current and scan rate, a and b are adjustable parameters[41]. Typically, $b = 0.5$ means that the process is totally governed by diffusion, while $b = 1.0$ suggests the capacitive behavior. As plotted and fitted in Fig. 3b, the as-calculated b value for peaks 1–4 are 0.78, 0.86, 0.79, and 0.81, respectively, revealing that the electrochemical process of the V_2O_5@rGO-1.5 is monopolize-dominated by the capacitive process along with partial diffusion contribution. Moreover, the detail contribution of such two processes can be clarified by the following relationship:[42]

$$i = i_{cap} + i_{diff} = k_1\upsilon + k_2\upsilon^{1/2} \tag{2}$$

As specifically shown in Supplementary Fig. 12, a high capacitive contribution of 80.8% can be achieved at the scan rate of $1.0\,\mathrm{mV\,s^{-1}}$. Moreover, the contribution ratio of the capacitive process shows a gradual increase trend from 0.1 to $1.0\,\mathrm{mV\,s^{-1}}$ (Fig. 3c). The capacitance dominated process in each scan rate is in line with the result discussed above. Meanwhile, the GITT was used to investigate the Zn^{2+} diffusion coefficient in electrodes to highlight the structural merits of V_2O_5@rGO-1.5 nanocomposite in Zn-based

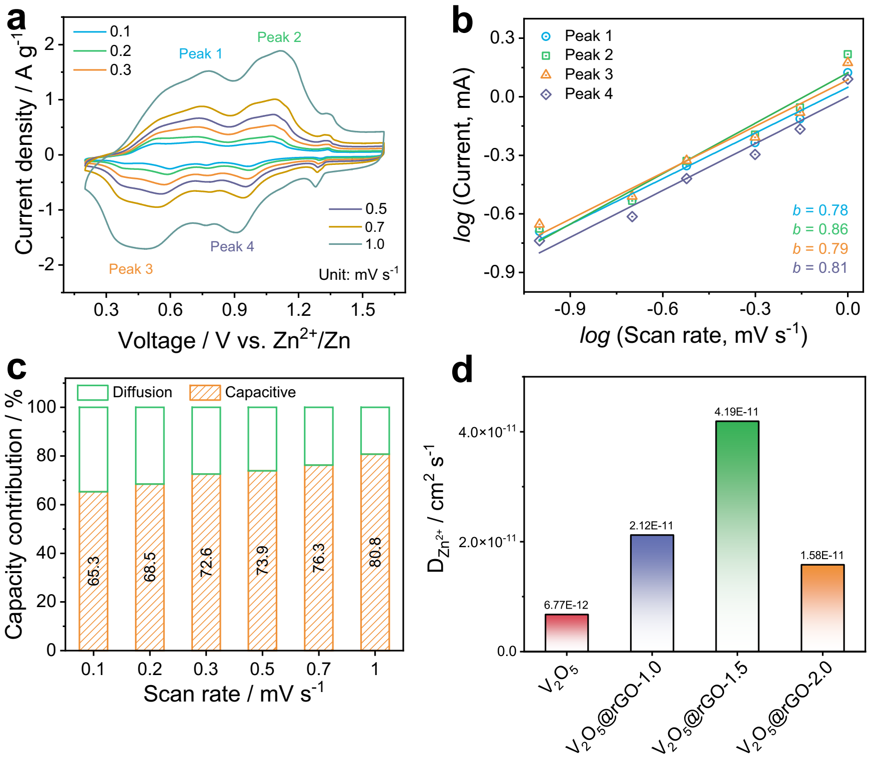

Fig. 3 | Electrochemical kinetics analysis of V_2O_5@rGO-1.5. **a** CV curves at different scan rates. **b** *log* (Current) *vs.* *log* (Scan rate) of various peaks, **c** the capacity contribution proportion at various scan rates. **d** Zn^{2+} diffusion coefficient obtained by GITT curves at charging/discharging.

thermoelectrochemical devices. The corresponding GITT curves during charging and discharging processes are displayed in Supplementary Fig. 23. Accordingly, the Zn^{2+} diffusion coefficient (D_{Zn}) of V_2O_5 is in a range of 10^{-12} to 10^{-11} cm^2 s^{-1} during the whole electrochemical tests (Supplementary Fig. 23a, e), demonstrating relatively sluggish insertion/extraction of Zn^{2+} in the pristine V_2O_5. With the increase of rGO content, the D_{Zn} value can be enhanced to a range of 10^{-11} to 10^{-10} cm^2 s^{-1} for V_2O_5@rGO-1.0 and V_2O_5@rGO-1.5 (Supplementary Fig. 23b, f and c, g), which is almost an order of magnitude higher than the value of V_2O_5. However, the D_{Zn} value shows a slight loss in the V_2O_5@rGO-2.0 (Supplementary Fig. 23d and h), which mainly caused by the dense wrapping of VO_x species by stacked rGO layers. As summarized in Fig. 3d, V_2O_5@rGO-1.5 exhibits the highest average Zn^{2+} diffusion coefficient of 4.19×10^{-11} cm^2 s^{-1} during the whole electrochemical processes. Such relatively fast insertion/extraction of Zn^{2+} in the V_2O_5@rGO-1.5 electrode may be owing to the relatively large interlayer spacing of $V_2O_5{\cdot}1.6H_2O$ and the high conductivity of rGO substrate. Most importantly, the crystal water may not only effectively reduce energy barrier but also mask the electrostatic interaction of Zn^{2+} via solvation effect[43–45]. The slightly low D_{Zn} value of charging part implies the sluggish extraction kinetics of Zn^{2+} from cathode, which requires high energy input to realize such charging procedure. Based on this feature, high efficiency and density can be achieved for the conversion from low-grade heat to electricity by using V_2O_5@rGO-1.5 based ZTCCs.

Energy conversion and storage behaviors

As attractive system integrated energy conversion and storage, the zinc ion batteries (ZIBs) are assembled to evaluate the electrochemical performances. Notably, the V_2O_5@rGO-1.5 based ZIBs shows superior rate capability (Supplementary Fig. 24a), in which 375.5, 383.5, 376.9, 353.4, 320.4, 266.3, 208.0, and 145.0 mAh g^{-1} can be recorded at 0.1, 0.2, 0.5, 1.0, 2.0, 5.0, 10.0, and 20.0 A g^{-1}, respectively. Impressively, the reversible discharging capacity can be nearly stabilized at 402.8 mAh g^{-1} as the current density recovers to 0.1 A g^{-1}. The slight increase of specific capacity after test could be caused by the electrolyte penetration induced activation process[35]. The rate performance of V_2O_5@rGO-1.5 cathode is also better than that of rGO, V_2O_5, V_2O_5@rGO-1.0, V_2O_5@rGO-2.0 electrodes and some of previously reposted materials (Supplementary Fig. 25a), such as VO_2-PC (82.6 mAh g^{-1} at 20 A g^{-1})[27], VPMX73 (282.2 mAh g^{-1} at 3 A g^{-1})[46], ZVO (167 mAh g^{-1} at 15 A g^{-1})[47], $Zn_{0.25}V_2O_5{\cdot}nH_2O$ (183 mAh g^{-1} at 6 A g^{-1})[43], MnVO (214 mAh g^{-1} at 8 A g^{-1})[31], $Ni_{0.25}V_2O_5{\cdot}nH_2O$ (164 mAh g^{-1} at 5 A g^{-1})[48], NVO/CNTs (203 mAh g^{-1} at 4 A g^{-1})[49], NaCaVO (154 mAh g^{-1} at 5 A g^{-1})[45], and $V_2O_5{\cdot}1.6H_2O$/MXene (81.2 mAh g^{-1} at 2 A g^{-1})[50]. As plotted in Supplementary Fig. 25b, the V_2O_5@rGO-1.5 based devices exhibits the highest energy density of 265 Wh kg^{-1} at a power density of 151 W kg^{-1} based on the active mass loading of cathode. Even under the highest power density of 12964.3 W kg^{-1}, a high energy density of 84.7 Wh kg^{-1} still can be retained, suggesting the superior energy storage behavior and rate capability of V_2O_5@rGO-1.5 among other electrode materials. Supplementary Fig. 24b displays the specific capacity retention of various electrodes at the current density of 10 A g^{-1}. Initially, the capacity of V_2O_5@rGO-1.5 increases to 195 mAh g^{-1} due to the gradual activation. Such value can maintain about 122 mAh g^{-1} even over 5000 cycles together with the corresponding Coulombic efficiency of ~100%, suggesting satisfying long cyclic stability. Notably, an obvious increase of capacity before 2000 cycles can be found in V_2O_5 cathode, this may be caused by the electrochemical activation process. However, large capacity decay of V_2O_5 cathode in following cycles may be caused by the dissolution of vanadium. Similar phenomenon can be found in V_2O_5@rGO-1.0 cathode. In addition, the cycled V_2O_5 electrode shows a distinct morphology change due to the obvious vanadium dissolution (Supplementary Fig. 26a). The cycled rGO electrode still holds the inter-connected morphology with abundant pores (Supplementary Fig. 26b), in line with its initial morphology. In sharp contrast, the cycled V_2O_5@rGO-x electrodes display similar structure and morphology to their pristine state (Supplementary Fig. 26c–e), and rGO layers can be visually observed in each electrode. From the EDX mapping images of each electrode after cycling, we can find that the zinc species exhibit in all electrodes due to the irreversible electrochemical reactions. Notably, both V_2O_5@rGO-2.0 and V_2O_5@rGO-1.5 electrodes present the relatively uniform distribution of C, O, Zn, and V elements (Supplementary Fig. 26d, e), demonstrating the effect of rGO to suppress the vanadium dissolution. However, the distribution of C and V in cycled V_2O_5@rGO-1.0 electrode is relatively uneven, which may be caused by the dissolution of vanadium. Therefore, both the V_2O_5@rGO-2.0 and V_2O_5@rGO-1.5 electrodes can achieve good stability when comparing with the V_2O_5@rGO-1.0 electrode. As plotted in Supplementary Fig. 27, the Seebeck coefficient value of each system by re-using cycled electrodes is relatively lower than that using fresh working electrodes. Especially, the ultralow Seebeck coefficient of $0.75 \pm 0.1\,\mathrm{mV\,K^{-1}}$ of pristine V_2O_5 is mainly caused by the serious dissolution of vanadium species during long-term cycling tests. However, the ZTCC with cycled V_2O_5@rGO-1.5 still can deliver a relatively high Seebeck coefficient of $17.5 \pm 2.6\,\mathrm{mV\,K^{-1}}$, further demonstrating that the rGO coating on V_2O_5 nanobelt shows key role to achieve satisfying durability and stability of vanadium-based devices by suppressing the dissolution of vanadium species to electrolyte. It should point out that the slight decrease of Seebeck coefficient value for V_2O_5@rGO-1.0, V_2O_5@rGO-1.5, V_2O_5@rGO-2.0, and rGO based ZTCCs could be the influence of byproducts.

Besides, various temperatures from 30 °C to 50 °C were adopted to further investigate the merits of heterostructure. With the increase of testing temperature (30 °C and 40 °C), the specific capacity of all cathodes can be enhanced and the electrochemical activation process can be accelerated due to the thoroughly infiltration of electrolytes (Supplementary Fig. 24c, d). It is worth mentioning that the V_2O_5@rGO-2.0 cathode exhibits better rate capability and cycling stability than other electrodes at 40 °C (Supplementary Fig. 24e, f), which is mainly attributed to its lowest dissolution rate of vanadium into electrolyte among other materials. Apart from the dissolution of vanadium, the dendrite growth and byproduct formation on Zn-G anode under relatively high temperatures (50 °C) would become the culprit of cell failure. Worthily, all as-assembled cells will be short-circuited when the total testing time is around 80 h (Supplementary Fig. 24g, h). Even vanadium dissolution at high temperatures will intensify, the cells should be operated with relatively low capacity rather than short-circuited. Thus, the biggest issue of Zn-based cells under high temperatures could be the serious growth of dendrite.

Furthermore, only a low absolute temperature coefficient of $2.5\,\mathrm{mV\,K^{-1}}$ can be obtained from the CV curves of as-developed V_2O_5@rGO-1.5 based ZTCC, which is much lower than the Seebeck coefficient ($23.4 \pm 1.5\,\mathrm{mV\,K^{-1}}$). Such relatively small polarization potential (~50 mV) indicates the fast electron transfer kinetics and the better reversibility of ZTCCs. Noted from equation S7 in Supplementary Note 2, in addition to the tested temperature coefficient, some possible factors also could affect thermopower or Seebeck coefficient of ZTCCs. The first one is related to the entropy change of redox species. The second one is the concentration difference of redox species in ZTCCs, which greatly impacts the whole Seebeck coefficient due to the possible chemical reactions between the two electrodes. The last one is the thermodiffusion of electrolyte ions in ZTCCs. Meanwhile, the CV curves of both H-type ZTCCs under different temperature differences and coin-type cells under various temperatures indicate the polarization of redox reactions between V_2O_5 and Zn can be significantly optimized by adding moderate rGO (Supplementary Note 2, Supplementary Figs. 28 and 29).

To well understand the energy conversion and storage mechanism of ZTCC, we observed the morphology change of both V_2O_5@rGO-1.5 cathode and Zn-G anode during the thermoelectrochemical measurements by SEM. As shown in Supplementary Fig. 30a1, the V_2O_5@rGO-1.5 is evenly wrapped by carbon black and PVDF in the initial electrode. After discharging to 0.2 V, some thin films were covered on the surface of the electrode along with the Zn^{2+} insertion to the V_2O_5@rGO-1.5 cathode (Supplementary Fig. 30a2), which may be caused by the generation of by-product like $Zn_4(CF_3SO_3)_4(OH)_4{\cdot}3H_2O$. Notably, as-formed film can be gradually decomposed with the increase of temperature difference from 5 to 30 K (Supplementary Fig. 30a3–a8). Moreover, the graphite layers are covered on the surface Zn-G (Supplementary Fig. 30b1), implying the successful modification of pure Zn anode[37]. Even discharged to 0.2 V (Zn^{2+} ions are stripped from the Zn-G anode), the graphite layers still can be maintained on the surface of Zn-G (Supplementary Fig. 30b2). Worthily, the morphology of Zn-G anode during the whole thermoelectrochemical process changes obviously. When the temperature difference is 5 K (Supplementary Fig. 30b3), some byproducts nucleate on the surface of Zn-G anode with the plating of Zn^{2+}. Furthermore, the Zn-G anode displays a well-defined array structure formed by numerous thin nanosheets (Supplementary Fig. 30b4–b8). We also conducted structural characterizations of V_2O_5@rGO-1.5 cathode during various charge/discharge states with ex-situ XRD and XPS analyses to investigate such processes. Specifically, the V_2O_5@rGO-1.5 electrode at different voltages is marked as adopted temperature differences (x K) and state y, as depicted in Fig. 4a. It should point out that the sharp peaks at ~26.4° and 54.5° in all XRD patterns correspond to the graphite substrate (Fig. 4b and c). Compared to the initial electrode, the pattern of the electrode at 0.2 V after the first discharge shows the obvious right shift of characteristic peak, suggesting the transformation of the electrode from $V_2O_5{\cdot}1.6H_2O$ to $Zn_xV_2O_5{\cdot}nH_2O$ due to the co-insertion of Zn^{2+} and H_2O[46]. During the thermal charge process, the (001) plane of $Zn_xV_2O_5{\cdot}nH_2O$ gradually shifts to a low-angle region and shows a tendency to change back to $V_2O_5{\cdot}1.6H_2O$ (Fig. 4b), indicating the thermoextraction of Zn^{2+}/H_2O from crystals. Moreover, the formed $Zn_xV_2O_5{\cdot}nH_2O$ almost fully recovers as $V_2O_5{\cdot}1.6H_2O$ (state I) after the following electrochemically charging process to 1.6 V (Fig. 4c). Notably, the reversible shift of (001) plane from state I to state V well confirms the highly reversible conversion between $Zn_xV_2O_5{\cdot}nH_2O$ and $V_2O_5{\cdot}1.6H_2O$, demonstrating high reversibility for energy storage. This phenomenon also suggests the co-insertion of Zn^{2+} and H_2O into $V_2O_5{\cdot}1.6H_2O$ during the discharging process, which then adjusts back to $V_2O_5{\cdot}1.6H_2O$ owing to the extraction of ions during the following charging process. Notably, the weak peak around 17.1° during the thermoelectrochemical process can be attributed to the presence of $Zn_4(CF_3SO_3)_4(OH)_4{\cdot}3H_2O$, confirming the formation of byproduct on electrode surface[42,51,52].

The chemical states and electronic interaction during fully charge and discharge stages are further investigated by using XPS measurements (Fig. 4d–f). As shown in Fig. 4d, two strong peaks located at 1022 and 1045 eV from state III can be assigned to the Zn $2p_{3/2}$ and Zn $2p_{1/2}$ signals, which is reasonably caused by the insertion of Zn^{2+} into the vanadium oxide layers. After charging to state V, the Zn $2p$ signals with lower intensity indicate that a lot of Zn^{2+} can be reversibly extracted, while partial residual zinc species still present in V_2O_5@rGO-1.5 cathode[35]. When considering the valence change of V element during electrochemical processes, the electrode at state III shows a strong V^{4+} peak together with a high V^{4+}/V^{5+} ratio of 1.06, meaning a significant reduction of V_2O_5 with the insertion of Zn^{2+} (Fig. 4e). Upon recharging to state V, the V^{5+} peak becomes strong and the V^{4+}/V^{5+} ratio (0.31) is almost recovered to the initial state (0.23), in consistent with the extraction of Zn^{2+}. In addition, the content of H_2O in O 1s spectra exhibits significant change after discharge and charge (Fig. 4f), confirming the solvation effect endowed insertion of H_2O associated with the major insertion of Zn^{2+}[43]. According to the above results, the possible electrochemical reactions can be proposed as follows:

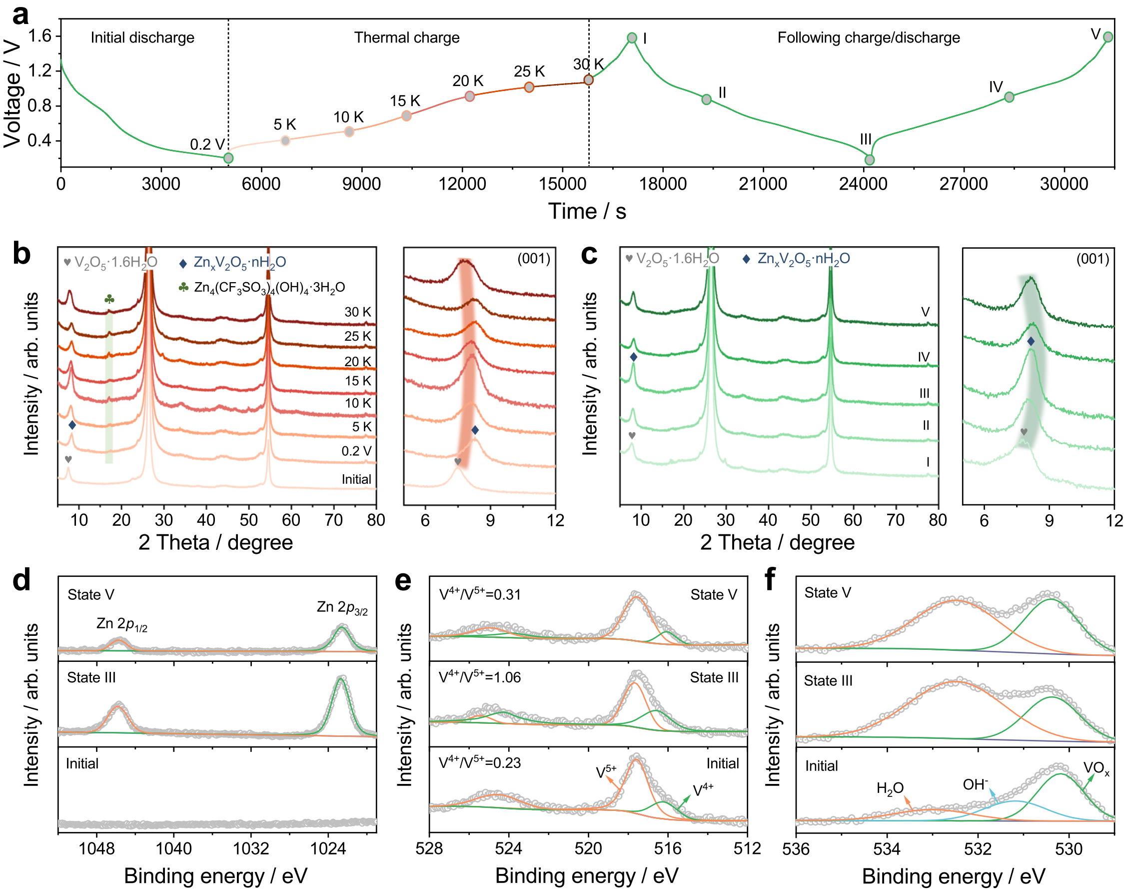

Fig. 4 | The mechanism analyses of V_2O_5@rGO-1.5 based ZTCCs. **a** The voltage change curves at different processes. **b**, **c** The corresponding ex-situ XRD patterns of V_2O_5@rGO-1.5 cathode during **b** thermal charging states at various temperature differences and **c** electrochemically charging/discharging states at 30 K. **d**–**f** The corresponding ex-situ XPS spectra of **d** Zn 2*p*, **e** V 2*p*, and **f** O 1*s*.

Cathode:

$$V_2O_51.6H_2O + xZn^{2+} + 4H^+ + (n-1.6)H_2O + 2xe^- \leftrightarrow H_4Zn_xV_2O_5{\cdot}nH_2O \quad (3)$$

$$4H_2O \leftrightarrow 4H^+ + 4OH^- \quad (4)$$

$$2Zn^{2+} + 2Zn(CF_3SO_3)_2 + 4OH^- + 3H_2O \leftrightarrow Zn_4(CF_3SO_3)_4(OH)_4{\cdot}3H_2O \quad (5)$$

Anode:

$$xZn \leftrightarrow xZn^{2+} + 2xe^- \quad (6)$$

Demonstration of wearable devices

Quasi-solid-state devices shows great promise in multi-functional applications due to their flexibility, safety, and wearability[53]. Here, the wearable ZTCC was using polyacrylamide (PAM) based gel electrolyte, which is sandwiched by Zn-G anode and V_2O_5@rGO-1.5 cathode, as illustrated in Supplementary Fig. 31. It is worth mentioning that the temperature difference between two electrodes is generated by a resistive heater (12 V, 7 W) attached on the cathode side. The as-assembled device delivers the output voltage of 0.38 V at an ultralow temperature difference of 8 K among other solid-state devices (Fig. 5a). After deducting the self-charging contribution (Supplementary Fig. 32), the thermal-induced voltage is 55, 74, 89, 101, 111, 117, 126, and 122 mV at the temperature difference from 1 to 8 K, respectively. As summarized in Fig. 5b, the corresponding Seebeck coefficient of V_2O_5@rGO-1.5 based solid-state device is calculated to be around 11.9 ± 1 mV K^{-1}, reflecting good thermal-electrical response in near room temperature low-grade heat harvesting. Such value also is much higher than that of rGO (10.4 ± 1 mV K^{-1}), V_2O_5 (8.9 ± 1 mV K^{-1}), V_2O_5@rGO-1.0 (5.2 ± 0.7 mV K^{-1}), and V_2O_5@rGO-2.0 (9.4 ± 0.7 mV K^{-1}) based devices. Remarkably, the highest thermal-induced power density of 0.12 W m^{-2} can be obtained by V_2O_5@rGO-1.5 among all as-fabricated solid-state devices (Fig. 5c), signifying an ultrahigh normalized power density of 1.9 mW m^{-2} K^{-2} in state-of-the-art reported systems (Supplementary Table 1). Inspired by such impressive performances of V_2O_5@rGO-1.5 based solid-state ZTCC, an external load with a resistance of 10 kΩ was employed to examine its stability and durability in energy conversion. As displayed in Fig. 5d, the output voltage was stably maintained at ~0.4 V with the adoption of temperature gradient, implying the satisfying thermal stability and promise potential of solid-state ZTCC. However, the relatively high voltage decay of rGO and V_2O_5 based solid-state ZTCC are possibly caused by the poor capacity and sluggish ion diffusion kinetics, respectively. In contrast, the slight voltage changes of V_2O_5@rGO-1.0 and V_2O_5@rGO-2.0 based solid-state ZTCC could be attributed to their relatively low ion diffusion coefficient. Even after 7 days, the V_2O_5@rGO-1.5 based solid-state ZTCC still can realize the thermal charge and discharge processes (Supplementary Fig. 33). This result demonstrates that as-developed ZTCCs can be used repetitively for relatively long-term cycling rather than being a one-time energy source. As a demo, three ZTCCs connected in series can easily light up a white light-emitting diode (LED) with a temperature difference of ~10 K (Fig. 5e). When considering the temperature difference between body

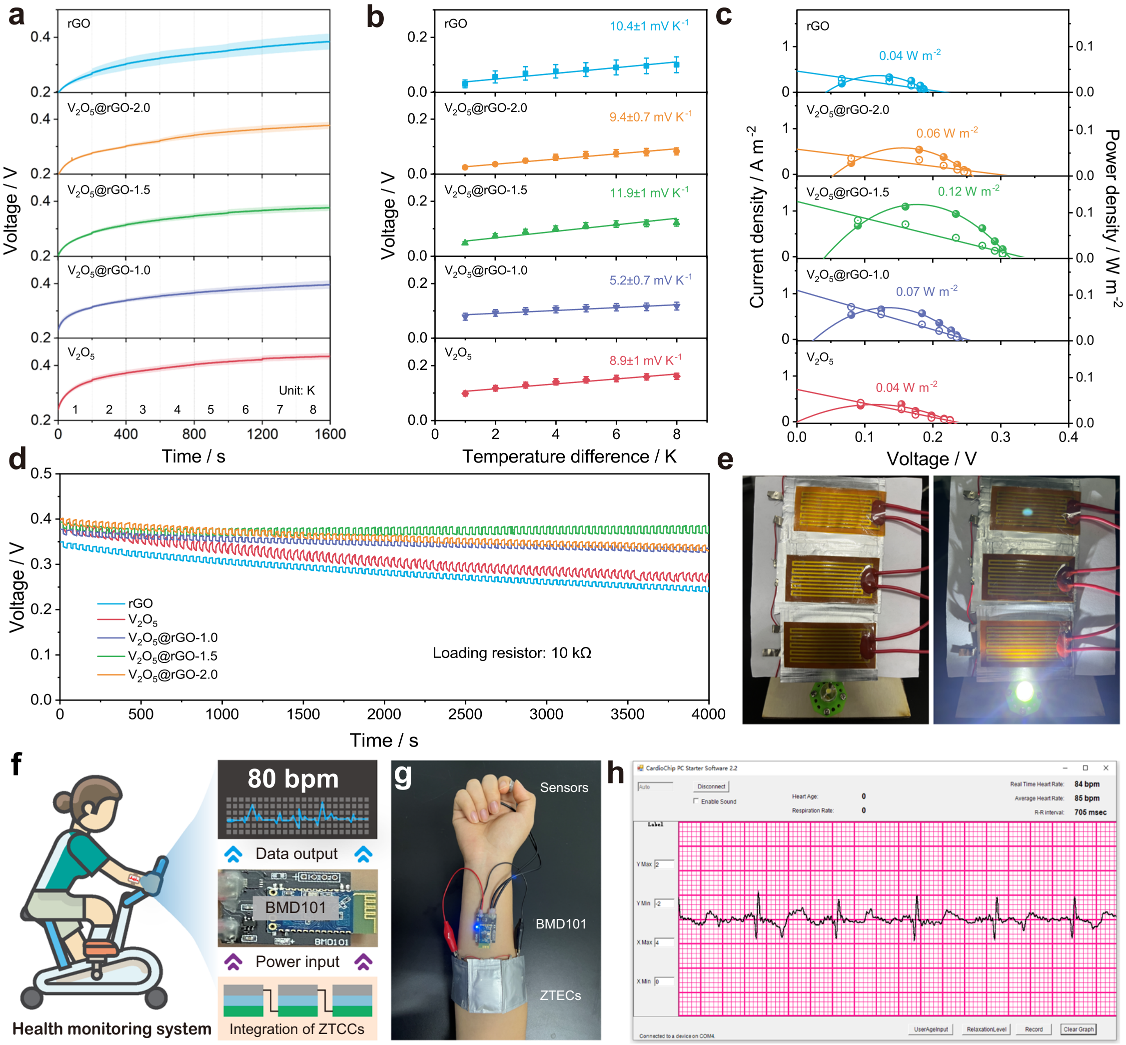

Auto
☐ Enable Sound
Heart Age: 0
Respiration Rate: 0
Real Time Heart Rate: 84 bpm
Average Heart Rate: 85 bpm
R-R interval: 705 msec
Y Max 2
Y Min -2
X Max 4
X Min 0
Connected to a device on COM4

Fig. 5 | Construction of quasi-solid-state ZTCCs using PAM based gel electrolyte and applications. **a** Thermal charging curves under various temperature differences. **b** Fitted Seebeck coefficient. **c** Thermal-induced current density (hollow symbol) and power density (solid symbol). **d** Thermal stability with a loading resistance of 10 kΩ. **e** Digital photo of a white LED lighted by three ZTCCs in series. **f** Illustration for health monitoring system. **g** Body heat-charged health monitoring system and **h** the recorded data.

heat and ambient, V_2O_5@rGO-1.5 based solid-state ZTCC is very attractive as one of power input source to replace traditional batteries for integrated health monitoring systems (Fig. 5f). Figure 5g shows the digital photo of a brief health monitoring system. Typically, the selected electro-cadiography sensor module (BMD101) can be powered by three ZTCCs connected in series. By Bluetooth wireless, the recorded data can be presented and processed in the mobile phone or laptop (Fig. 5h). All above-mentioned demonstrations further confirm the application prospect of as-constructed ZTCCs in energy conversion and storage fields, which makes it possible in terms of electronics integration.

Discussion

In summary, this work has developed high-performance ZTCCs by cathode engineering. By sequentially introducing 2D rGO into 1D $V_2O_5{\cdot}1.6H_2O$ nanobelts, both the thermal response and kinetics of as-constructed ZTCCs are modified. Notably, the $V_2O_5{\cdot}1.6H_2O$ nanobelts provide enough electroactive sites for dense Zn^{2+} storage, suggesting high capacity and energy density. The rGO layers wrapped around $V_2O_5{\cdot}1.6H_2O$ nanobelts can not only keep structural stability and inhibit V dissolution, but also accelerate the charge transfer, implying good durability and excellent power density. As a result, a giant thermopower of 23.4 ± 1.5 mV K^{-1} can be achieved by V_2O_5@rGO-1.5 based ZTCC, which synergistically integrates the fast thermodiffusion and thermoextraction processes. Moreover, a high thermal-induced voltage of 0.72 V and normalized power density of 1.04 mW m^{-2} K^{-2} can be delivered at the temperature difference of 30 K. The ex-situ experiments and DFT calculations reveal that the rGO can boost the charge transfer at the heterointerfaces formed by rGO and $V_2O_5{\cdot}1.6H_2O$. Besides, the crystal water layer in $V_2O_5{\cdot}1.6H_2O$ can promote the diffusion of Zn^{2+} with low energy barrier due to its reduced electrostatic repulsion effect. It is worth mentioning that as-proposed V_2O_5@rGO-1.5 based ZTCC shows great promise in self-power supply for health monitoring systems. By coupling with hydrogel electrolyte, three solid-state ZTCCs attached to the arm can drive the Bluetooth wireless module by an ultralow temperature difference formed between body heat and atmosphere, demonstrating potential application of ZTCCs in energy conversion and storage as well as wearable electronics areas.

Methods

Preparation of V_2O_5@rGO-x

To prepare V_2O_5@rGO-x, the concentration of commercial graphene oxide (GO, CARMERY, Institute of Coal Chemistry, Chinese Academy of Sciences) solution was firstly adjusted to 1.0, 1.5, and 2.0 mg mL^{-1}. Then, 120 mg of vanadium pentoxide (V_2O_5, Xiya Reagent) was dissolved in 60 mL of GO solution and stirred magnetically for about 30 min at room temperature. Subsequently, above solution was transferred into a 100 mL Teflon-lined stainless steel autoclave and kept at 180 °C for 12 h. Finally, the products were collected by centrifugation at 9166 RCF xg for 3 min and washed several times using deionized water and ethanol, followed by drying overnight. The samples are labeled as V_2O_5@rGO-x, where x represents the GO concentration. For comparison, we carried out control experiments with pure GO solution (1.5 mg mL^{-1}) and V_2O_5 in water by the same conditions to obtain rGO and V_2O_5, respectively.

Material characterizations

The morphology was observed by using a field emission scanning electron microscope (FESEM, FEI NANO SEM430) and a high-resolution transmission electron microscope (HRTEM, JEOL JEM-2100). X-ray diffraction (XRD) patterns were recorded from PANalytical Empyrean diffractometer with Cu Kα radiation (λ = 1.5406 Å). The surface chemical states of samples were detected by X-ray photoelectron spectrometer (XPS, Thermo Scientific K-Alpha). The Raman spectra were collected by the Horiba Scientific LabRAM HR with an excitation wavelength of 532 nm. Thermogravimetric analysis (TGA) curve was recorded on a Mettler-Toledo STARe SW 15.00 analyzer with a heating rate of 10 °C min^{-1} under air flow. The wettability of materials was measured by a CA tester (XG-CAMC33) using electrolyte drop (10 μL). The dissolution rate of vanadium into electrolyte was detected by Inductively Coupled Plasma Optical Emission spectroscopy (ICP-OES, Thermo Fisher iCAP PRO). The SSA of samples were measured by the ASAP 2460 analyzer (micromeritics), and were analyzed by Brunauer-Emmett-Teller (BET) method.

Electrochemical measurements

Thermoelectrochemical performance tests of ZTCCs were conducted in a non-isothermal H-type cell with 0.5 mol L^{-1} $Zn(CF_3SO_3)_2$ electrolyte on a standard electrochemical workstation (CHI 760E). Zn-G foil (thickness: ~20 μm) and as-prepared electrodes were used as counter/reference electrodes and working electrodes, respectively. The Zn-G anode was modified by graphite using the pencil drawing method. To prepare the working electrode, V_2O_5@rGO-x, acetylene black, and polyvinylidene fluoride were firstly mixed together in a mass ratio of 7:2:1. Then, the slurry was painted on graphite paper with a diameter of 1.2 cm (mass loading: 1.2 mg cm^{-2}) as working electrode. CV curves of ZIBs were recorded from 0.1 to 1.0 mV s^{-1} with a voltage window of 0.2–1.6 V by the Biologic VMP-300 workstation. GITT, rate capability, and cyclic stability were measured using the CT3001A Land Battery Test System.

The quasi-solid-state ZTCC was assembled by Zn-G foil anode and V_2O_5@rGO-x cathode together with hydrogel electrolyte. It should mention that both the Zn-G and V_2O_5@rGO-x electrodes hold the area of 2×3 cm^2, and the active mass loading in the V_2O_5@rGO-x electrode is about 8 mg. In addition, the PAM gel electrolyte was prepared by following steps. 2 g of acrylamide (AM, Macklin) and 0.4 g of acrylic acid (AA, Macklin) were dispersed into 10 mL mixed solvent of deionized water and glycerol in a volume ratio of 1:2. Subsequently, 1.5 mg of *N*,*N*′-methylenebisacrylamide (Macklin), 10 μL of *N*,*N*,*N*′,*N*′-tetramethylethylenediamine (Aladdin), and 0.25 g of potassium persulfate (Aladdin) were added into above solution part by part with vigorous stirring for 4 h under ice-water bath. After that, the transparent solution was injected in a mold and polymerized by using a UV lamp (365 nm, 60 W) for 20 min to prepare the hydrogel matrix. Moreover, such hydrogel soaked with 0.5 mol L^{-1} $Zn(CF_3SO_3)_2$ electrolytes can be used for the construction of quasi-solid-state ZTCCs.

Data availability

All relevant data that support the findings of this study are presented in the manuscript and supplementary information file. Source data are available from the corresponding author upon reasonable request.

References

1. Tarascon, J. M. et al. Issues and challenges facing rechargeable lithium batteries. *Nature* **414**, 359–367 (2001).
2. Zhao, Z. et al. Designing flexible, smart and self-sustainable supercapacitors for portable/wearable electronics: From conductive polymers. *Chem. Soc. Rev.* **50**, 12702–12743 (2021).
3. Liu, R. et al. Flexible self-charging power sources. *Nat. Rev. Mater.* **7**, 870–886 (2022).
4. Liu, H. et al. Hybrid energy harvesting technology: From materials, structural design, system integration to applications. *Renew. Sust. Energ. Rev.* **137**, 110473 (2021).
5. Shi, X. L. et al. Advanced thermoelectric design: From materials and structures to devices. *Chem. Rev.* **120**, 7399–7515 (2020).
6. Pu, X. et al. Toward wearable self-charging power systems: The integration of energy-harvesting and storage devices. *Small* **14**, 1702817 (2018).
7. He, J. et al. Advances in thermoelectric materials research: Looking back and moving forward. *Science* **357**, eaak9997 (2017).
8. Yin, L. et al. Designing wearable microgrids: Towards autonomous sustainable on-body energy management. *Energy Environ. Sci.* **15**, 82–101 (2022).
9. Yan, Q. et al. High-performance thermoelectrics and challenges for practical devices. *Nat. Mater.* **21**, 503–513 (2022).
10. Zhang, S. et al. 3D-printed wearable electrochemical energy devices. *Adv. funct. mater.* **32**, 2103092 (2021).
11. Yang, Q. et al. Flexible thermoelectrics based onductile semiconductors. *Science* **377**, 854–858 (2022).
12. Shi, X. et al. Thermopower and harvesting heat. *Science* **371**, 343–344 (2021).
13. Massetti, M. et al. Unconventional thermoelectric materials for energy harvesting and sensing applications. *Chem. Rev.* **121**, 12465–12547 (2021).
14. Liu, Y. et al. Thermo-electrochemical cells for heat to electricity conversion: From mechanisms, materials, strategies to applications. *Energy Environ. Sci.* **15**, 3670–3687 (2022).
15. Han, C. G. et al. Giant thermopower of ionic gelatin near room temperature. *Science* **368**, 1091–1098 (2020).
16. Liu, S. et al. Giant and bidirectionally tunable thermopower in nonaqueous ionogels enabled by selective ion doping. *Sci. Adv.* **8**, eabj3019 (2022).
17. Han, Y. et al. High-thermopower polarized electrolytes enabled by methylcellulose for low-grade heat harvesting. *Sci. Adv.* **8**, eabl5318 (2022).
18. Yu, B. et al. Thermosensitive crystallization-boosted liquid thermocells for low-grade heat harvesting. *Science* **370**, 342–346 (2020).
19. Li, M. et al. High-efficiency thermocells driven by thermo-electrochemical processes. *Trends Chem.* **3**, 561–574 (2021).
20. Liu, C. et al. Ion regulation in double-network hydrogel module with ultrahigh thermopower for low-grade heat harvesting. *Nano Energy* **92**, 106738 (2022).
21. Zhou, J. et al. Interfacial architecting with anion treatment for enhanced thermoelectric power of flexible ternary polymer nanocomposites. *J. Mater. Chem. A* **9**, 20544–20552 (2021).
22. Zhao, W. et al. Chemical doping of organic semiconductors for thermoelectric applications. *Chem. Soc. Rev.* **49**, 7210–7228 (2020).
23. Liu, Y. et al. Advanced wearable thermocells for body heat harvesting. *Adv. Energy Mater.* **10**, 2002539 (2020).
24. Wang, X. et al. Direct thermal charging cell for converting low-grade heat to electricity. *Nat. Commun.* **10**, 4151 (2019).
25. Romano, M. S. et al. Carbon nanotube-reduced graphene oxide composites for thermal energy harvesting applications. *Adv. Mater.* **25**, 6602–6606 (2013).
26. Im, H. et al. High-efficiency electrochemical thermal energy harvester using carbon nanotube aerogel sheet electrodes. *Nat. Commun.* **7**, 10600 (2016).

27. Li, Z. et al. Zinc ion thermal charging cell for low-grade heat conversion and energy storage. *Nat. Commun.* **13**, 132 (2022).
28. Zhang, N. et al. Materials chemistry for rechargeable zinc-ion batteries. *Chem. Soc. Rev.* **49**, 4203–4219 (2020).
29. Blanc, L. E. et al. Scientific challenges for the implementation of Zn-ion batteries. *Joule* **4**, 771–799 (2020).
30. Zhu, H. et al. Magnetocaloric effects in a freestanding and flexible graphene-based superlattice synthesized with a spatially confined reaction. *Nat. Commun.* **5**, 3960 (2014).
31. Liu, C. et al. Expanded hydrated vanadate for high-performance aqueous zinc-ion batteries. *Energy Environ. Sci.* **12**, 2273–2285 (2019).
32. Dong, S. et al. Ultra-fast NH_4^+ storage: Strong H bonding between NH_4^+ and bi-layered V_2O_5. *Chem* **5**, 1537–1551 (2019).
33. Yan, B. et al. Single-crystalline V_2O_5 ultralong nanoribbon waveguides. *Adv. Mater.* **21**, 2436–2440 (2009).
34. Li, G. et al. High-efficiency cryo-thermocells assembled with anisotropic holey graphene aerogel electrodes and a eutectic redox electrolyte. *Adv. Mater.* **31**, e1901403 (2019).
35. Li, Z. et al. Microstructural engineering of hydrated vanadium pentoxide for boosted zinc ion thermoelectrochemical cells. *J. Mater. Chem. A* **10**, 21446–21455 (2022).
36. Lu, Y. et al. High energy-power Zn-ion hybrid supercapacitors enabled by layered B/N co-doped carbon cathode. *Nano Energy* **66**, 104132 (2019).
37. Li, Z. et al. Pencil drawing stable interface for reversible and durable aqueous zinc-ion batteries. *Adv. Funct. Mater.* **31**, 2006495 (2020).
38. Zhang, Y. et al. A chemically self-charging aqueous zinc-ion battery. *Nat. Commun.* **11**, 2199 (2020).
39. An, Y. et al. Thermally chargeable proton capacitor based on redox-active effect for energy storage and low-grade heat conversion. *Energy Environ. Mater.* **6**, e12305 (2023).
40. Li, Y. et al. Realizing record-high output power in flexible gelatin/GTA-KCl-$FeCN^{4-/3-}$ ionic thermoelectric cells enable by enlarging working temperature range. *Energy Environ. Sci.* **15**, 5379–5390 (2022).
41. Lindström, H. et al. Li^+ ion insertion in TiO_2 (Anatase). 2. Voltammetry on nanoporous films. *J. Phys. Chem. B* **101**, 7717–7722 (1997).
42. Li, Z. et al. Flexible and anti-freezing quasi-solid-state zinc ion hybrid supercapacitors based on pencil shavings derived porous carbon. *Energy Storage Mater.* **28**, 307–314 (2020).
43. Kundu, D. et al. A high-capacity and long-life aqueous rechargeable zinc battery using a metal oxide intercalation cathode. *Nat. Energy* **1**, 16119 (2016).
44. Yan, M. et al. Water-lubricated intercalation in $V_2O_5 \cdot nH_2O$ for high-capacity and high-rate aqueous rechargeable zinc batteries. *Adv. Mater.* **30**, 1703725 (2018).
45. Zhu, K. et al. $NaCa_{0.6}V_6O_{16} \cdot 3H_2O$ as an ultra-stable cathode for Zn-ion batteries: The roles of pre-inserted dual-cations and structural water in V_3O_8 layer. *Adv. Energy Mater.* **9**, 1901968 (2019).
46. Liu, H. et al. Van der Waals interaction-driven self-assembly of V_2O_5 nanoplates and Mxene for high-performing zinc-ion batteries by suppressing vanadium dissolution. *ACS Nano* **16**, 14539–14548 (2022).
47. Zhu, K. et al. Hewettite $ZnV_6O_{16} \cdot 8H_2O$ with remarkably stable layers and ultralarge interlayer spacing for high-performance aqueous Zn-ion batteries. *Angew. Chem. Int. Ed.* **135**, e202213368 (2023).
48. Li, J. et al. Multi-scale investigations of δ-$Ni_{0.25}V_2O_5 \cdot nH_2O$ cathode materials in aqueous zinc-ion batteries. *Adv. Energy Mater.* **10**, 2000058 (2020).
49. Jiang, Y. et al. Spontaneous knitting behavior of 6.7-nm thin $(NH_4)_{0.38}V_2O_5$ nano-ribbons for binder-free zinc-ion batteries. *Energy Storage Mater.* **42**, 286–294 (2021).
50. Mei, Y. et al. Suppressing vanadium dissolution in 2D V_2O_5/MXene heterostructures via organic/aqueous hybrid electrolyte for stable zinc ion batteries. *Chem. Eng. J.* **452**, 139574 (2023).
51. Wang, L. et al. Ultralong cycle stability of aqueous zinc-ion batteries with zinc vanadium oxide cathodes. *Sci. Adv.* **5**, eaax4279 (2019).
52. Qi, Y. et al. Towards high-performance aqueous zinc-ion battery via cesium ion intercalated vanadium oxide nanorods. *Chem. Eng. J.* **442**, 136349 (2022).
53. Tian, R. et al. Body heat powers future electronic skins. *Joule* **3**, 1399–1403 (2019).

Acknowledgements

This work was supported by the Leading Edge Technology of Jiangsu Province (BK20220009-X.Z., BK20202008-X.Z.) and Priority Academic Program Development of Jiangsu Higher Education Institutions (PAPD). We thank Qian Zhu, Xiuwen Wang, Zhenxiao Ling (Nanjing University of Aeronautics and Astronautics) for their kind help. We thank the Center for Microscopy and Analysis at the Nanjing University of Aeronautics and Astronautics for the advanced facilities.

Author contributions

Z.L. carried out the experiment. Z.L., Y.X. and J.C. evaluated the electrochemical performances. L.W. analyzed the structural characterization and electrochemical results. Z.L. and Y.X. organized the figures. H.D. and X.Z. supervised the whole work. All authors co-discussed the results and wrote the manuscript.

Competing interests

The authors declare no competing interests.

Additional information

Supplementary information The online version contains supplementary material available at https://doi.org/10.1038/s41467-023-42492-z.

Correspondence and requests for materials should be addressed to Xiaogang Zhang.

Peer review information *Nature Communications* thanks Peihua Yang and the other anonymous reviewer(s) for their contribution to the peer review of this work. A peer review file is available.